Contents lists available at ScienceDirect

Soil Dynamics and Earthquake Engineering

Regional spectral characteristics, quality factor and site responses in western-central Sichuan, China (II): Application to stochastic ground motion simulation

Pengfei Dang [a,b,*], Hongfeng Yang [b,d,**], Jie Cui [a], Jian Song [c]

[a] *School of Civil Engineering, Guangzhou University, Guangzhou, China*
[b] *Earth and Environmental Sciences Programme, Faculty of Science, The Chinese University of Hong Kong, Shatin, NT, Hong Kong, China*
[c] *Guangdong Hualu Transportation Technology Co., Ltd, Guangzhou, China*
[d] *Shenzhen Research Institute, The Chinese University of Hong Kong, Shenzhen, Guangdong, China*

ARTICLE INFO

ABSTRACT

The stochastic finite-fault approach was used to model the 2022 Luding earthquake with a magnitude of Mw 6.6 in China at 16 selected near-field stations. To investigate the impact of the site effect on the synthetic results, two models were taken into account: One model was obtained from the generalized inversion technique, and the other model was obtained from the horizontal-to-vertical spectral ratio method. The high-frequency attenuation parameter was estimated to be 0.040 s and the value of 4.0 MPa for the stress parameter was adopted. Comparisons of the recorded and simulated Fourier amplitude spectrum, pseudospectral acceleration, peak ground acceleration, and peak ground velocity were performed to investigate the capability of the selected input parameters. In addition, the model bias, simulated peak ground acceleration and peak ground velocity were calculated by the local site amplification estimated by the two methods. The results show that the site effects estimated by the generalized inversion technique can well simulate the high-frequency response spectra and Fourier amplitude spectrum and can provide peak ground acceleration and peak ground velocity values consistent with the recorded values, while the local site amplification roughly calculated by the horizontal-to-vertical ratio method underestimates the main ground motion characteristics. Furthermore, strong-motion records with the same magnitude but different hypocentral distance ranges in the generalized inversion technique are used to estimate near-surface site effects, which shows that the distance range has a small impact on the estimation of local site amplification. Model parameters that performed well in this study provide confidence in understanding and quantifying seismic hazards in the Luding area from earthquake scenarios with different magnitudes.

1. Introduction

It is widely known that local site conditions can influence the amplitude level, frequency content and duration of ground motion caused by earthquakes. The scaling laws of earthquake source parameters and site responses, which play crucial roles in developing ground motion attenuation relationships and simulating near-field ground motions, are closely related to earthquake prediction and seismic hazard assessment. Likewise, in an increasing number of scientific and technological studies on earthquake analysis, the necessity of determining the local site effects for the seismic resistance of structures has been well

recognized [1]. However, there are many factors that control the calculation of the site effect, such as topography, sediment-bedrock interface geometry, sediment thickness and nonlinear characteristics of the site [2]. As such, it is nontrivial to accurately obtain the site effect. For soft soil sites, the impact of the local site effect estimated by different methods on the results of near-field ground motion simulation is a key issue that we closely monitored in this study because if the site effects are under- or overestimated or even ignored, they may lead to a strong bias in simulating earthquake ground motions. However, if there is no good information on the lithology beneath the station, determining site effects requires a large number of strong-motion recordings from

* Corresponding author. School of Civil Engineering, Guangzhou University, Guangzhou, China.
** Corresponding author.
E-mail addresses: iempengfeid@gzhu.edu.cn (P. Dang), hyang@cuhk.edu.hk (H. Yang), jcui@gzhu.edu.cn (J. Cui), 913606737@qq.com (J. Song).

earthquakes, which were not available in various regions, such as Sichuan, China, despite the high earthquake risk in those locations.

Before the 2008 Wenchuan earthquake, strong-motion recordings were very scarce in China. During the Wenchuan mainshock, the China Strong Motion Network Center (CSMNC) obtained approximately 1400 sets of high-quality strong-motion acceleration data for the mainshock. In the past decade, the CSMNC obtained multiple sets of three-component recordings, including those for the 2008 Wenchuan earthquake of **M** = 8.0, 2013 Lushan earthquake of **M** = 7.0 and 2017 Jiuzhaigou earthquake of **M** = 7.0. These abundant strong-motion observation data provide a good foundation for studying the site effects in western Sichuan, China. The site amplification factors used in the stochastic finite-fault technique include crustal and local site amplification coefficients. Site effects are used to describe the shallow site amplification and damping effects and can be calculated by the quarter-wavelength method [3,4] that requires detailed drilling data, the H/V spectral ratio approach (HVSR) [5] or the parametric generalized inversion technique (GIT) [6–8]. When regional drilling data is lacking, the H/V or GIT is considered to be the most direct method for estimating the local site amplification. In the ground motion simulation, the H/V method is widely used to approximately estimate the site effect because it is simple and easy to perform. However, it is well known that the site amplification estimated by the H/V spectral ratio can only approximately obtain the predominant frequency but may underestimate the amplification peak of the site [9–13]. For comparison purposes, the site effects obtained from the H/V spectral ratio are also displayed. Therefore, both site effect models have been adopted in the following section to model source inversions by the stochastic finite-fault model (EXSIM), focusing on ground motion at high frequencies.

At present, there are many examples of applying GIT to a specific earthquake event in China [14–17]. However, there are few specialized studies that use a large number of historical strong-motion records to investigate site effects in a large specific region. In this study, we collected 2568 sets of observation records at 81 strong-motion stations that were generated by 161 earthquakes with magnitudes of 3.0–7.0. These events had hypocentral distances of 12–472 km in the Longmenshan fault zone and Anninghe fault zone. The peak ground accelerations (PGAs) in both horizontal components are between 2 and 100 cm/s^2 to avoid the nonlinear response of the soil layer. Various hypocentral distance ranges were adopted to study the impact of distance on the site amplification. Then, we determined the site effect for ground motion simulation that is applicable to western Sichuan by the GIT approach. Furthermore, to investigate the impact of site amplification obtained in this study and that estimated by the H/V spectral ratio on the simulation results, we modelled ground motion at 16 near-fault stations with hypocentral distances of <145 km triggered by the 2022 Luding earthquake using the EXSIM algorithm. Ground motion simulation at soft soil sites should consider local site effects, which can be obtained by the GIT and H/V methods. Our results can further improve the accuracy of earthquake ground motion simulation and indicate that if there is not enough data in the study area, site effects can be estimated using seismic records from nearby areas [18,19].

2. Method and data

Since there are several assumptions, such as a very specific geometric spreading function and functional shape of quality factor, and a simple calculation process, site effect analysis approaches based on strong-motion data are increasingly recognized and widely used. Among these approaches, the parametric GIT proposed by Andrews [6] represents the Fourier amplitude spectrum (FAS) of ground motion recorded at the observation point as the product of three factors, namely, source, path, and site in the frequency domain:

$$FAS_{ij}(f) = S_i(f)G_i(f)GS(R_{ij})\exp\left(-\pi f R_{ij} / [Q(f)\beta]\right) \quad (1)$$

in which $S_i(f)$, $GS(R_{ij})$ and $G_j(f)$ represent the source spectrum of the ith event, geometric spreading function, and site effect at the jth station, respectively. $Q(f)$ indicates the quality factor, β represents the S-wave velocity and R_{ij} denotes the hypocentral distance (unit: km). The trade-off between the site and source components can be resolved by selecting a reference rock station where the local site amplification is determined [8,11,20].

2.1. Luding data

At 20:52 UTC on September 5, 2022 (12:52 on September, Beijing standard time), an earthquake of moment magnitude Mw 6.6 struck Luding County, Ganzi Tibetan Autonomous Prefecture, Sichuan Province, China. The epicenter was located at 29.59°N and 102.08°E, with a focal depth of 16 km, and was on the eastern boundary of the rhombic Sichuan-Yunnan block, near the Moxi fault in the southern part of the Xianshuihe fault zone [21] (Fig. 1). This fault segment is located at the intersection of the Xianshuihe fault, the Anninghe-Daliangshan fault, and the Longmenshan fault, and the tectonic structure is extremely complex [22,23]. The Sichuan Earthquake Administration reported that the maximum intensity of the Luding earthquake was IX according to the standard of the China Seismic Intensity Scale, and the affected area was approximately 280 km^2. Moreover, tens of thousands of buildings have been damaged, affecting the operation of local lifelines and facilities [24]. In addition, more than 5707 landslides caused by the Luding earthquake resulted in large economic losses and casualties [21,25]. As of 17:00 on September 11, the Luding earthquake had caused 93 deaths, and 25 people were missing [26]. Sichuan, located in the Southwest China, has witnessed many destructive earthquakes in the past few decades, such as the 1923 Luhuo earthquake of **M** = 7.3, the 1933 Diexi
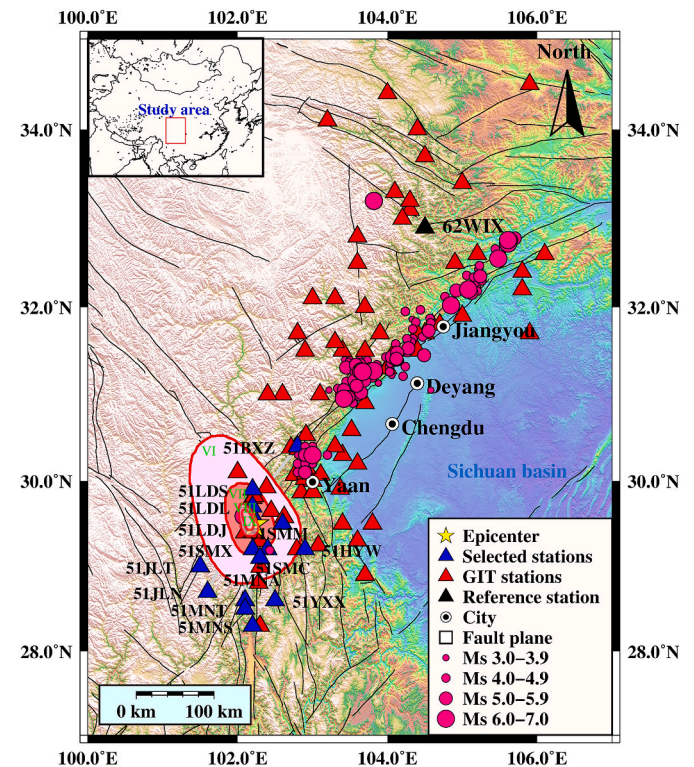

Fig. 1. Locations of the selected observation stations (blue triangles) and epicenter (yellow star) of the Luding earthquake in China. The black triangle shows the reference station, red triangles denote the stations used in the GIT method, and the deep pink circles represent the epicenters of the earthquake events. The macroseismic intensity map can be found on the website (see Data Availability). The inset map shows the location of the study area in China.

earthquake of **M** = 7.5, the 1973 Luhuo earthquake of **M** = 7.6, the 2008 Wenchuan earthquake of **M** = 8.0, the 2013 Lushan earthquake of **M** = 7.0 and the 2017 Jiuzhaigou earthquake of **M** = 7.0. These catastrophic earthquakes have caused significant casualties and property losses. Therefore, earthquake ground motion simulations have been widely used to estimate the impact of earthquakes. The simulation of ground motions is crucial for seismic design, risk assessment, postdisaster rescue, and disaster management [27]. Due to limited ground-motion records in certain regions, ground motion simulation is quite important for these areas, particularly for engineering applications that require a large amount of seismic data. Due to earthquakes being one of the most destructive natural disasters, they often cause casualties, structural damage, and huge economic losses. Accordingly, it is necessary to investigate ground motion to assess its impact on urban areas.

The Luding earthquake event was recorded at 63 strong-motion stations operated by the CSMNC. Among these near-field observation stations, only 16 stations with epicentral distances of <150 km were selected in our simulation, which were shown in Fig. 1 using blue triangles. Besides, the characteristics of these selected stations are summarized in Table 1. The acceleration waveforms profiles show that all the selected strong-motion stations are located at soft soil sites. For these stations, the generic soil amplification factors by Boore and Joyner [3] are adopted [28–30].

2.2. Data processing

After baseline correction of the raw data, a 4th-order Butterworth filter of 0.25–20 Hz was adopted to eliminate errors caused by instrument response and to limit the impact of the noise on ground-motion recordings. The shear-waves of the north-south (NS) and east-west (EW) components of the strong-motion records were extracted using a window function with lengths of 5–15 s [31–34]. Then, a cosine taper was used at the onset and offset of the shear-wave window, and the length of every taper was defined as 10% of the total waveform length [10,11]. Finally, the FAS obtained from each recording was smoothed with the bandwidth parameter $b = 20$ [11] for the smoothing window defined by Konno and Ohmachi [35].

2.3. Calculating the local site effect

In this study, we used the parametric GIT method to separate source spectra, path propagation and site effects. Equation (1) can be written in linear form by taking the natural logarithms on both sides:

$$\ln FAS_{ij}(f) - \ln GS(R_{ij}) = \ln S_i(f) + \ln G_i(f) - \pi f R_{ij} / [Q(f)\beta] \quad (2)$$

where $FAS_{ij}(f)$ can be obtained from the observed data and $GS(R_{ij})$ is defined by Boore [4]. In this case, the source spectra $S(f)$, quality factor $Q(f)$ and site effect function $G(f)$ on the right side can be calculated by solving Equation (2) with the singular value decomposition approach to remove the uncertain degree of freedom of Equation (2). Furthermore, Considering the lack of knowledge on velocity profiles, we also calculated the site effects by HVSR method. Even though it is generally believed that the HVSR approach underestimates the real site amplification [36,37], it is still commonly adopted to quickly portray the average frequency-amplification behavior [38]. Unlike horizontal ground motions, the amplification effect of site conditions on vertical ground motions are not significant [39–41], therefore, the H/V value can be obtained as follows [7]:

$$\frac{H}{V} = \sqrt{\frac{FAS_{EW}^2 + FAS_{NS}^2}{2 \times FAS_V^2}} \quad (3)$$

where FAS_{NS}, FAS_{EW} and FAS_V represent the horizontal (EW and NS) and vertical FAS, respectively. In some previous studies [12,13], the geometric mean of two components was used to calculate the H/V value, in fact, the difference between the geometric mean and vector sum of the NS and EW components is very small.

The detailed introduction of the GIT method and the principles of data selection have been introduced in the previous study related to western-central Sichuan, China [42], then, the source parameters and site amplification inverted by GIT were applied to model the Luding earthquake. In EXSIM simulation, the site amplification usually includes two types: crustal site amplification and local site amplification [4,28]. The regional site effects in ground motion simulation code (EXSIM) for soft soil sites was investigated when simulating the 2017 Jiuzhaigou earthquake of Mw = 6.6 and 2013 Lushan earthquake of Mw = 6.7 in China [43]. The results of the study show that crustal and local site amplification coefficients need to be considered in the EXSIM when the strong-motion stations are located at soft soil sites [44]. In the study area, there are no detailed S-wave profiles, therefore, the crustal site amplification for Class C sites was given by Boore and Joyner [3]. Recently, some studies reported that the terrain and local geological effects exist a considerably impact on seismic ground motion [45]. The acceleration waveform can be simulated at observation points by incorporating the influences of local site amplifications [46]. The complex geological environment usually generates a considerably complex seismic wave field, where many waves interfere with each other. This leads to the failure of the HVSR curve calculated by the S-wave to completely describe the complex local site response under the surface. Due to the lack of S-wave velocity data in the study area, we estimated a

Table 1
Information of the selected near-field observation stations triggered by the Luding earthquake.

No.	Station name	Longitude (°E)	Latitude (°N)	R (km)	PGA (cm/s²)		Site condition	Instrument type
					EW	NS		
1	51LDJ	102.2	29.6	11.65	110.17	306.07	Soil	ETNA/ES-T
2	51LDL	102.2	29.7	16.85	303.83	199.33	Soil	ETNA/ES-T
3	51LDS	102.2	29.9	36.36	62.93	44.92	Soil	ETNA/ES-T
4	51SMX	102.2	29.2	44.89	185.25	178.25	Soil	ETNA/ES-T
5	51SMM	102.4	29.2	53.30	394.68	317.00	Soil	ETNA/ES-T
6	51HYQ	102.6	29.5	51.28	46.91	76.75	Soil	ETNA/ES-T
7	51SMC	102.3	29.1	58.50	88.26	79.33	Soil	ETNA/ES-T
8	51JLT	101.5	29.0	86.40	127.75	147.05	Soil	ETNA/ES-T
9	51HYW	102.9	29.2	90.49	37.75	32.27	Soil	ETNA/ES-T
10	51JLN	101.6	28.7	109.37	69.40	88.88	Soil	ETNA/ES-T
11	51YXX	102.5	28.6	117.38	31.49	50.20	Soil	ETNA/ES-T
12	51MNA	102.1	28.6	110.08	26.05	29.13	Soil	ETNA/ES-T
13	51MNJ	102.1	28.5	121.19	25.20	16.79	Soil	ETNA/ES-T
14	51MNT	102.1	28.5	121.20	86.73	90.88	Soil	ETNA/ES-T
15	51BXZ	102.8	30.4	113.64	14.28	13.49	Soil	ETNA/ES-T
16	51MNS	102.2	28.3	143.89	14.01	14.18	Soil	ETNA/ES-T

Note: R represents the epicentral distance (km). The site conditions and instrument types can be obtained from the raw seismic record files.

mean value via the HVSR [5,46,47]. In this study, we used 2568 sets of strong-motion observation records from 81 stations recorded by 161 earthquakes with magnitudes of 3.0–7.0 and hypocentral distances of

12–472 km and obtained the site responses of 81 stations using the generalized inversion technique. Unlike the dataset in the previous study [42], the dataset used in this study includes earthquake records
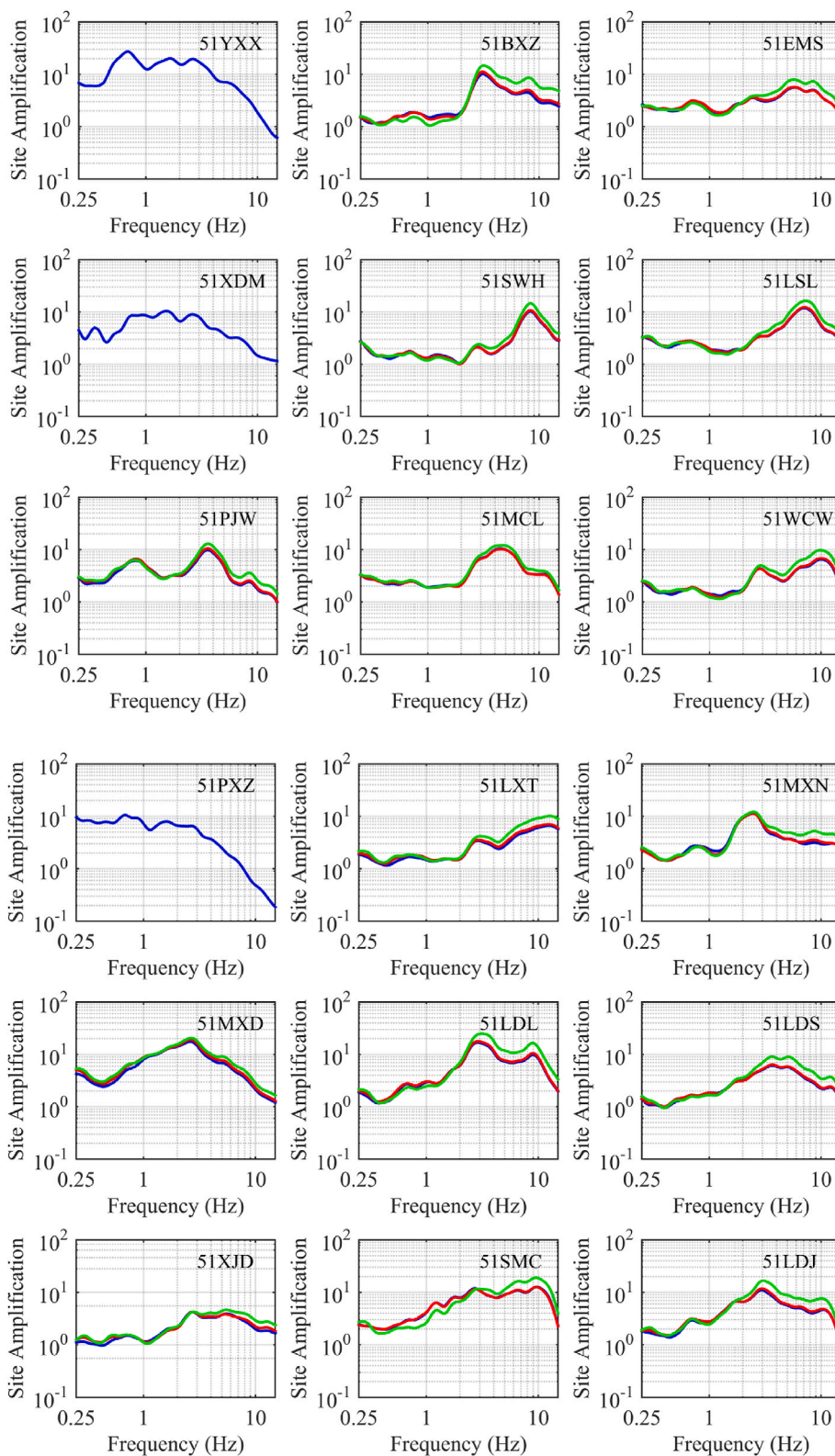

Fig. 2. Local site amplification functions of 80 stations obtained using the GIT method. Blue, red, and green solid lines represent the site amplification curves obtained from scheme 1 (hypocentral distance range: 12–472 km), scheme 2 (hypocentral distance range: 20–300 km) and scheme 3 (hypocentral distance range: 20–200 km), respectively. The blue curves of stations 51YXX, 51XDM, 51PXZ, 51MZQ, 51QCQ, 51LSH, 51QCD, 62TSH, 62MXT, and 51AXB indicate that the results are only obtained from scheme 1.
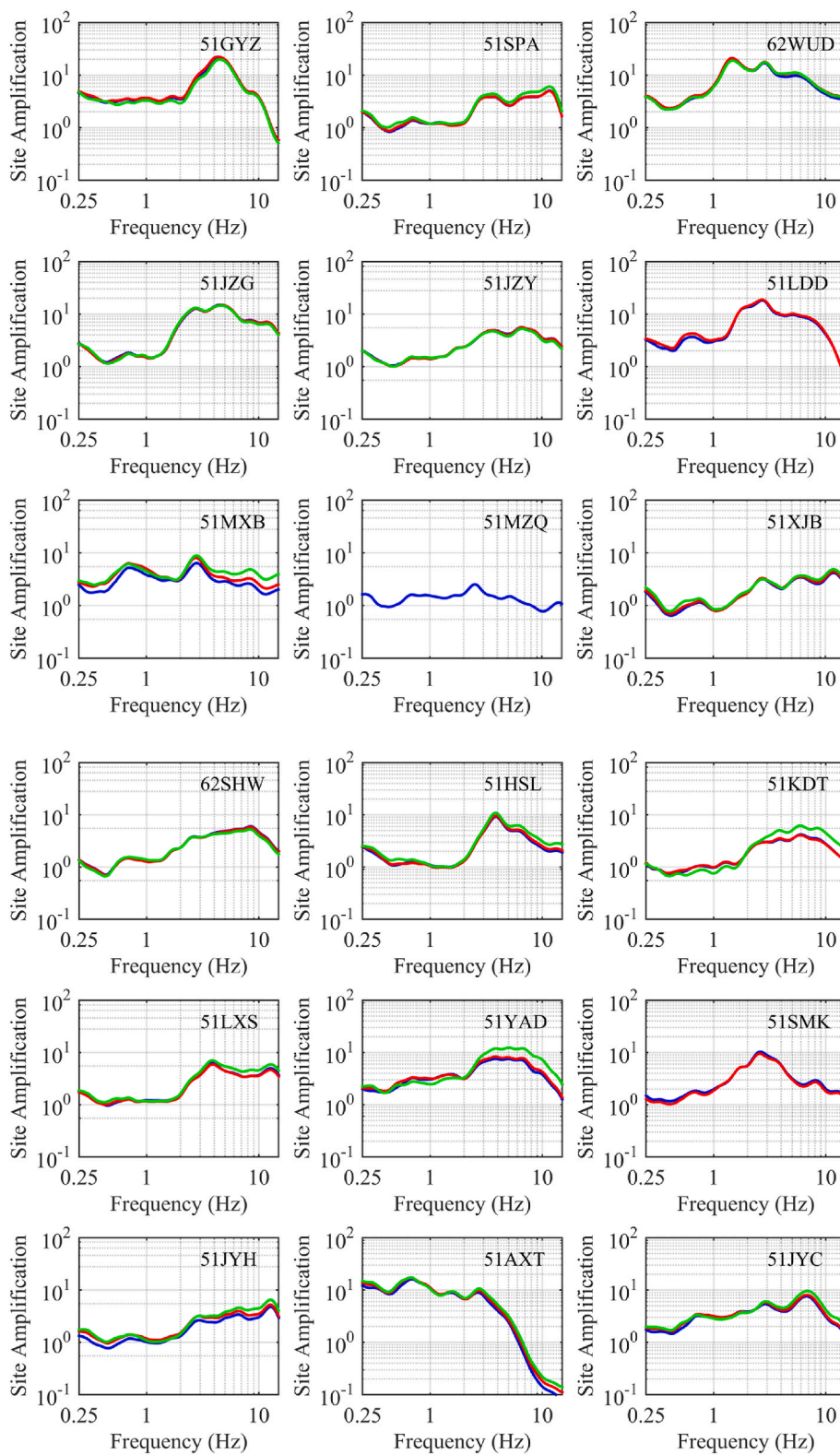
Fig. 2. (*continued*).

with magnitudes less than 4.0. Earthquakes with magnitudes less than 4.0 may cause instability in the inversion results of source parameters [48] but do not affect the estimation of site effects. The bedrock station 61WIX, which spectral ratio results indicating that the site effects are nearly constrained to be unity around all frequencies, is selected as the reference station [11,42,49]. In addition, to investigate the influence of the hypocentral distance range on the calculation of site response, different hypocentral distances (Scheme 1, *R* range: 12–472 km; Scheme 2: 20–200 km; Scheme 3: 20–300 km) were selected to estimate the local site effects using GIT method (Fig. 2). The results show that the local site response function obtained by different schemes has little difference, especially in the low frequency range. However, the high-frequency
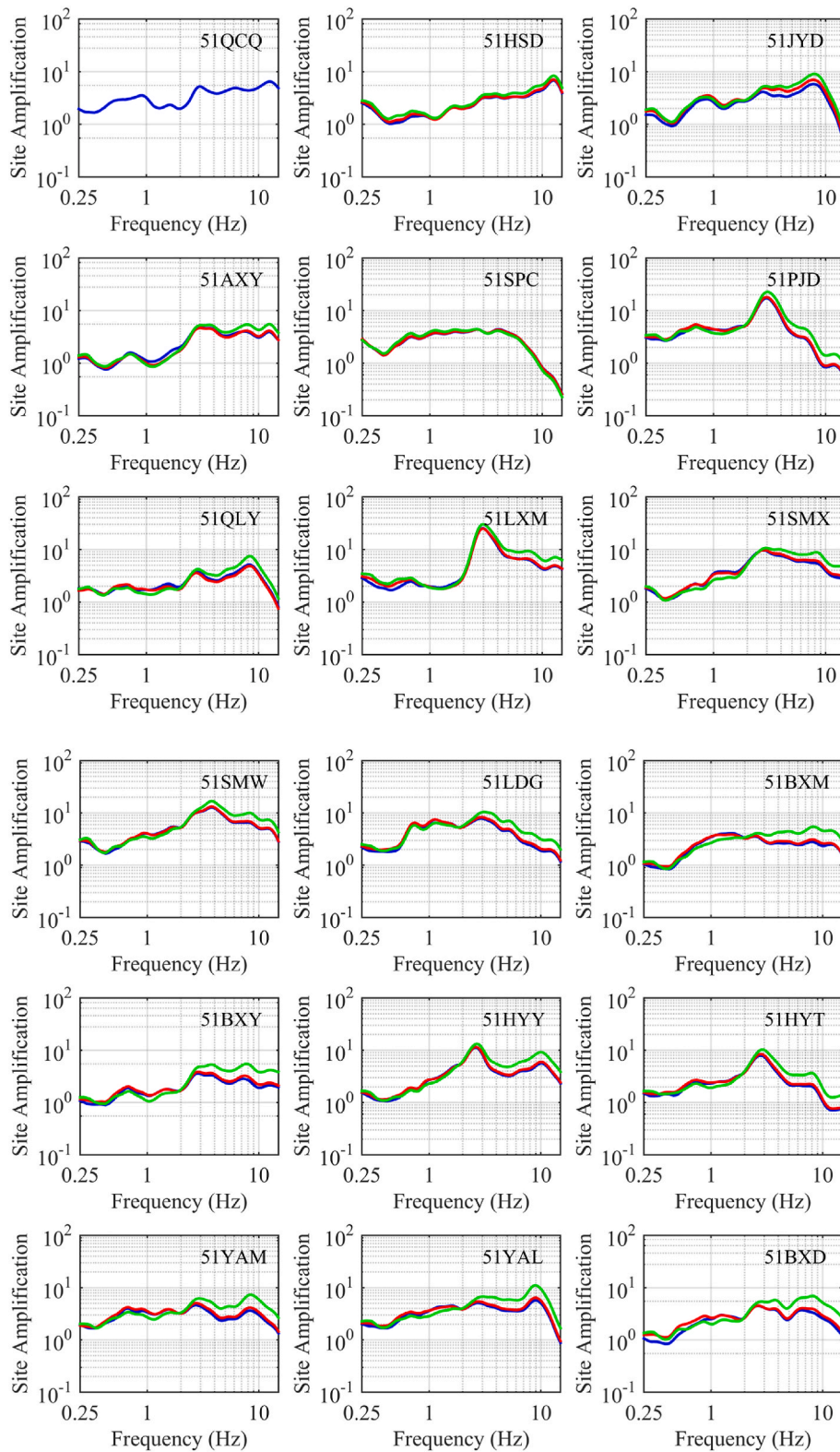
Fig. 2. (*continued*).

amplitude level has significant differences, especially at stations 51BXZ, 51EMS, 51SWH, 51LSL, 51WCW, 51LXT, 51MXN, 51LDL, 51LDS, 51LDJ, 51KDT, 51YAD, 51PJD, 51LDG, 51BXM, 51BXY, 51HYY, 51HYT, 51YAM, 51YAL, 51BXD, 51HYQ, 51YAS, 51JKH, 51TQD, and 51LSF. This may be due to the attenuation characteristics of seismic wave at high frequency band. The average value was then used as the

local site amplification factor. Fig. 3 shows the average site amplifications obtained from the GIT method based on different hypocentral distance ranges, indicating that the hypocentral distance has a weak dependence on the local site amplification near the surface. For comparison purpose, the H/V spectral ratios also are plotted. Although site-specific site amplifications may perform much better than the
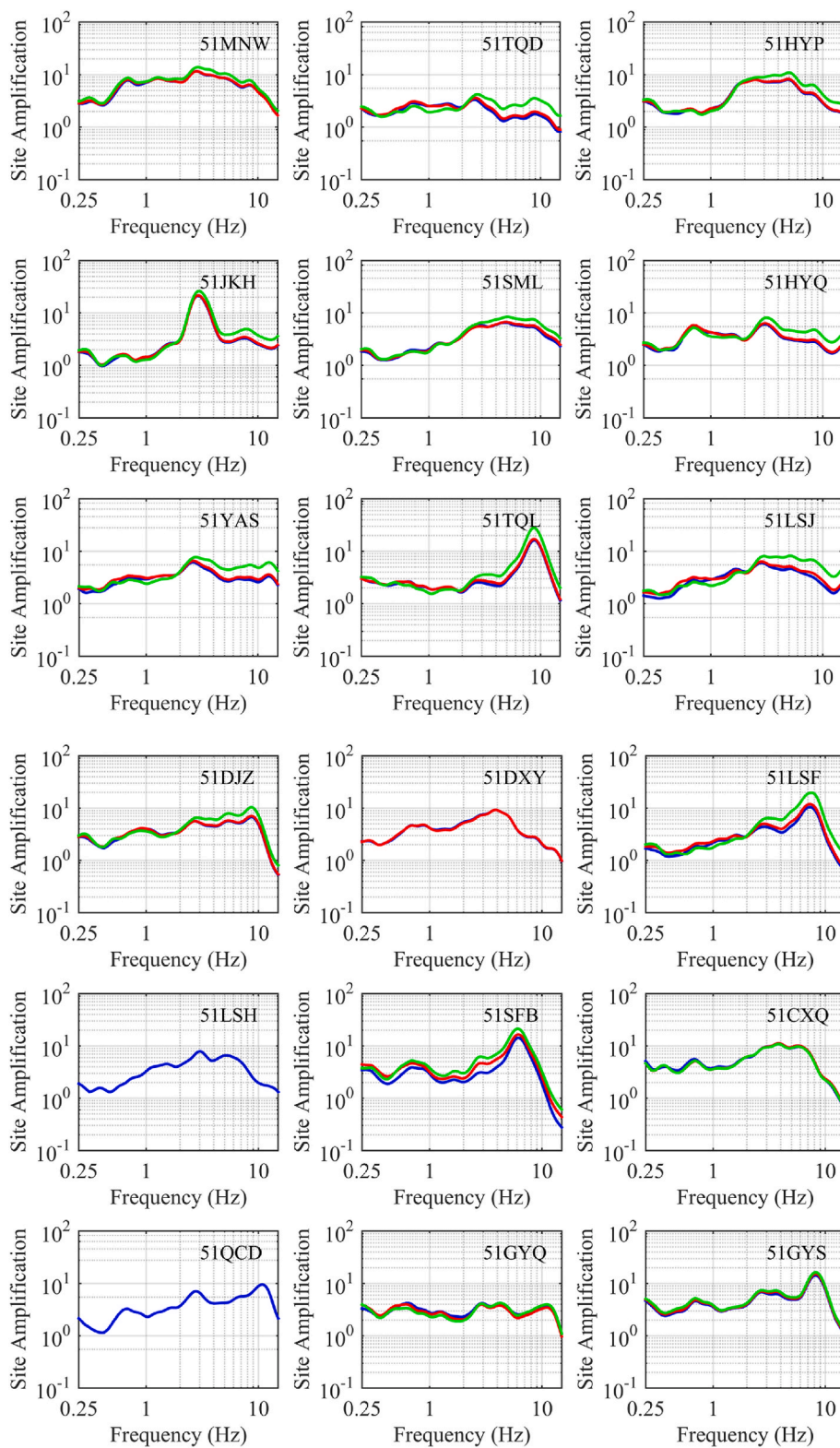
Fig. 2. (*continued*).

average one when comparing with the observed recording at each station [50,51], to better use the site effect to model the scenario earthquakes, finally, the average site effect model that calculated by the GIT and H/V methods were adopted to simulate the Luding earthquake at all stations [28,52] (Fig. 3).

3. Input parameters

EXSIM has been widely adopted to model the ground motion impacts of historical earthquakes [27,30,38,43,45,53–60]. The model parameters in EXSIM are critical for simulating earthquake ground motions, and the input parameters that were adopted in the EXSIM algorithm include source, path, and site components. In this study, the source parameters
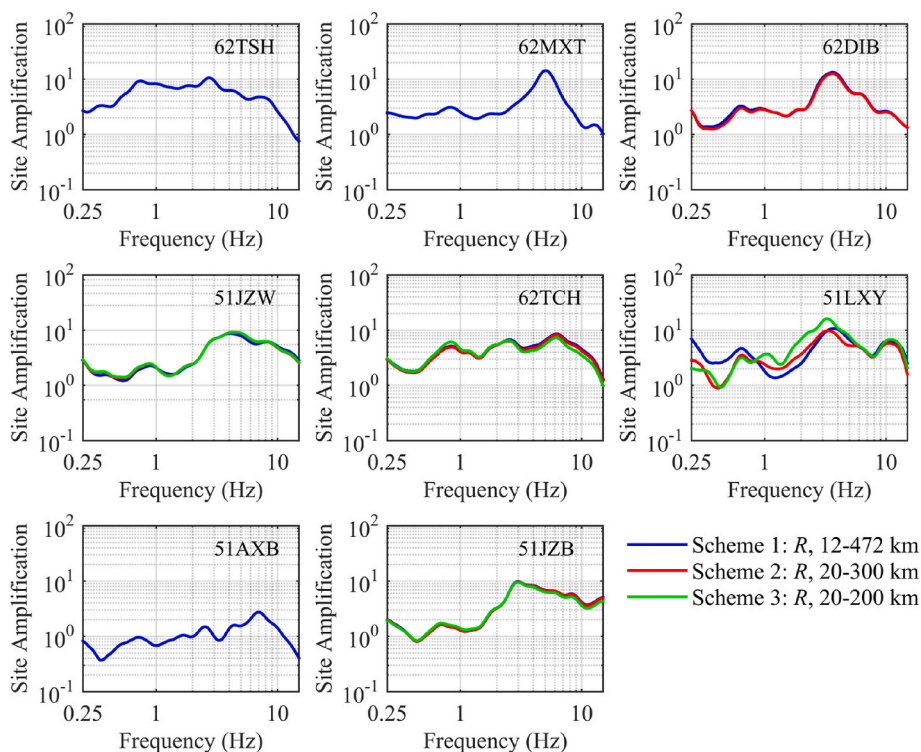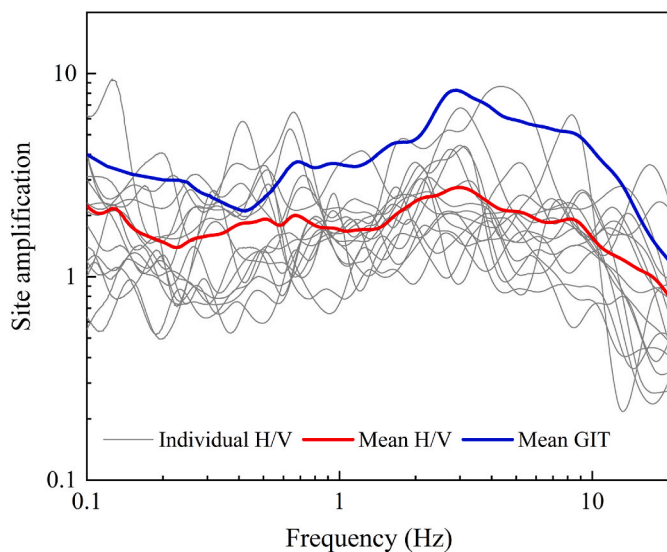
Fig. 2. (*continued*).

Fig. 3. Average site amplification used in this study. Blue and red solid lines indicate the site amplification estimated by the GIT and H/V spectral ratio methods, respectively. The grey solid lines indicate the H/V values estimated by each station.

Fig. 4. The slip distribution of the Luding earthquake given by Han et al. [60]. The rupture fault was characterized as 30 km × 16 km, and the maximum slip amount was 2.23 m.

were provided by a previous study [61]. In this slip model (Fig. 4), a fixed rupture velocity (0.8β) was used, the moment magnitude Mw is determined to be 6.6, and the spatial location of the main fault is modelled as $167.36°$ and $73.668°$ strike and dip, respectively. To investigate the impact of different source parameters on the synthetic results, seven source models with different size and slip distribution were adopted to model the Luding earthquake [62]. Their results showed that the location of the rupture initiation point and the asperity had a significant impact on the synthetic results. In addition, the deviation between the Han's model and the other six source models was not
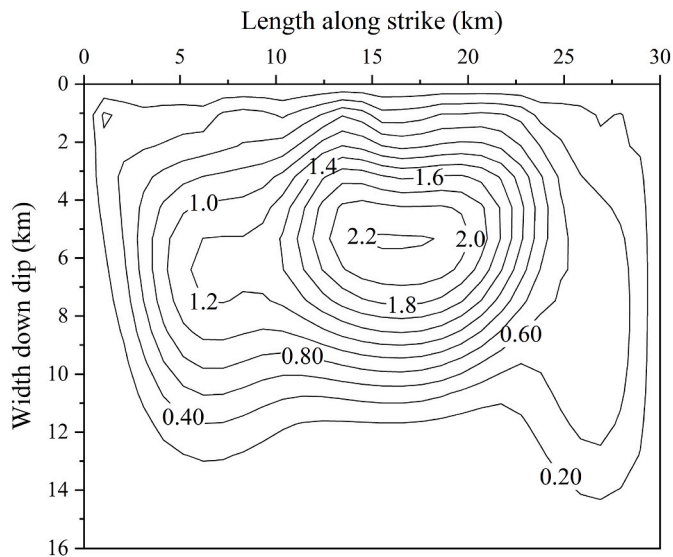
significant, indicating that the parameters provided by the Han's model can be used to model the Luding earthquake. Beresnev [63] claimed that the stress drop in Brune's model is not the true stress parameter in the tectonic zone near the source before and after the earthquake event, but rather a stress parameter that controls the level of Fourier spectrum high-frequency radiation energy, reflecting the maximum rate of rupture propagation. The stress drop value that controls the high-frequency spectra level was set to 40 bars by trial-and-error method in our scheme [64].

In the EXSIM model, the rupture propagates at a fixed velocity (0.8β) from the initiation point to the surrounding area, triggering the rupture

of the remaining subfaults on the main fault. Then, in the time domain, all the observation recordings can be modelled by the stochastic point-source model for each subfault, and the acceleration time series $a(t)$ obtained from all subfaults on the rupture fault is summed together to obtain the recording for the main rupture fault at the points.

In EXSIM, the path component, $P(R_{ij}, f)$ can be defined by Ref. [4]:

$$P(R_{ij}, f) = GS(R)\exp[-\pi f R / (Q(f)\beta)] \tag{4}$$

in Equation (4), $Q(f)$ can be written as $Q(f) = Q_0 f^{\eta}$, where Q_0 and η represent the quality factor and index, respectively. $GS(R)$ indicates the geometric attenuation term [4]. By comparing the differences between the simulated and recorded values obtained by different path durations, Dang et al. [65] and Dang et al. [66] pointed out that both the path duration fitted by seismic data and the path duration provided by Atkinson and Boore [67] can obtain ideal simulation results. In EXSIM, the widely used path duration model was also given by Atkinson and Boore [67], therefore, the path duration model given by Atkinson and Boore [67] was adopted in this simulation. Besides, the geometric spreading model in Sichuan region was written as $G(R) = 1/R$ for epicentral distances less than 70.5 km, $G(R) = 1/70.5$ for epicentral distances between 70.5 km and 117.5 km, and $G(R) = 1/R^{0.5}$ for epicentral distances larger than 117.5 km [62]. The model parameters in path term were adopted to express the propagation effects. The anelastic attenuation adopted in our simulation can be obtained by GIT method and can be written as $Q(f) = 327.8f^{0.591}$, which is basically consistent with the quality factor $Q(f) = 334.4f^{0.581}$ given by Qiao et al. [68] based on strong-motion data from northwest Sichuan.

In the ω^2-shaped source model defined by Brune [69], it is generally assumed that the spectral acceleration response is flat at frequencies above the corner frequency. Based on this assumption, a kappa model (κ) was used to define the deviation of observed spectra from Brune's model by fitting the high-frequency attenuation of the acceleration spectra, and κ has been confirmed to be unrelated to the magnitude of the earthquake event [70–72]. The spectral delay parameter (κ) is calculated individually for every selected strong-motion station and the regression results show that the kappa parameter was determined to be 0.04 s [64], which is basically consistent with the kappa value of 0.0471 given by Fu et al. [73] for the Longmenshan region. In this study, the kappa parameter used for simulating the spectral decay at high frequencies was set to the same value at all stations [28,38,58,74,75]. The detailed model parameters needed for ground motion simulation of the Luding, China, earthquake are summarized in Table 2.

4. Analysis and discussion

4.1. Comparison of the simulated FAS and pseudospectral acceleration (PSA)

We compared the synthetic results obtained from local site amplifications based on the HVSR and GIT. Figs. 5 and 6 show the simulated and recorded FAS and PSA values of 16 near-field stations, respectively. Fig. 5 indicates that the local site amplification function obtained from the GIT can well match the observed FAS, especially at stations 51LDL, 51SMX, 51SMM, 51HYQ, 51SMC, 51YXX, 51MNA, 51LDS and 51MNS. However, at station 51LDJ, the simulated FAS obtained from the HVSR is better matched with the observed FAS than that obtained from the GIT at high frequency ($f > 1$ Hz). In addition, the synthetic FAS differs greatly from the observed FAS at stations 51JLT with epicentral distance $R_{epi} = 86.40$ km, 51BXZ with epicentral distance $R_{epi} = 113.64$ km and 51JLN with epicentral distance $R_{epi} = 109.37$ km since the average local site amplifications used in this simulation cannot express the true site conditions below the station. At the remaining stations (51HYW [$R_{epi} = 90.49$ km], 51MNJ [$R_{epi} = 121.19$ km] and 51MNT [$R_{epi} = 121.20$ km]), the simulated FAS agrees well with the observed FAS at low frequencies with frequency f less than 1 Hz but differs greatly at high frequencies

Table 2
Input parameters used for the ground-motion simulation of the Luding earthquake in China.

Parameters	Values	References
Rupture fault strike and dip	167.36°, 73.668°	Han et al. [61]
Rupture fault size (km)	30 × 16	Han et al. [61]
Subfault size (km)	1 × 1	This study
Kappa parameter κ_0 (s)	0.04	Dang et al. [64]
Slip model	Inverted slip model	Han et al. [61]
Geometric attenuation model	1/R, R < 70.5 km 1/70.5, 70.5 ≤ R ≤ 117.5 km 1/$R^{0.5}$, R > 117.5 km	Dang et al. [50]
Path duration model	0, R < 10 km 0.16(R-1), 10 ≤ R < 70 km 9.6–0.03(R-70), 70 km ≤ R < 130 km 7.8 + 0.04(R-130), R ≥ 130 km	Atkinson and Boore [67]
Rise time	1/f_0 for EXSIM	Boore [29]
Crustal site amplification	NEHRP Class C for EXSIM	Boore and Joyner [3]
Pulsing area percentage	50%	Motazedian and Atkinson [28]
Frequency-related Quality factor	327.8 $f^{0.591}$	This study
Local site effects	H/V and GIT methods	This study
Stress drop (MPa)	8.0	Dang et al. [64]

with frequency f greater than 1 Hz, which may be caused by inappropriate high-frequency attenuation parameters (κ_0). Interestingly, these stations with poor simulation results are located within epicentral distances of 70 km and 120 km. Within this distance range, a constant geometric spreading coefficient (1/70.5) was adopted.

Fig. 6 shows that the simulated PSA values obtained from local site effect calculated by the GIT can better match the observed PSA at most of the selected near-field stations, especially at stations 51SMM, 51HYQ, 51SMC, 51HYW, 51YXX, 51MNA, 51MNJ, 51LDS, 51SMX, 51MNT and 51MNS. However, the simulated PSA obtained from local site effects calculated by the HVSR method underestimate the observed PSAs at these stations, especially in the long period, in which period T is greater than 1 s. In addition, at two near-field stations, 51LDJ ($R_{epi} = 11.65$ km) and 51LDL ($R_{epi} = 16.85$ km), there are significant differences between the simulated and observed PSA values. This may result from the nonlinear characteristics of the site [21] and the rupture directivity effect. The PGA values recorded for the two horizontal components at station 51LDJ and 51LDL are 110.17 cm/s^2 (EW) and 306.07 cm/s^2 (NS) and 303.83 cm/s^2 (EW) and 199.33 cm/s^2 (NS), respectively, which shows obvious rupture directivity characteristics. At the remaining stations, such as 51JLT, 51JLN and 51BXZ, the simulated PSA values differ greatly from the recorded values, which exhibit similar characteristics to the simulated FAS. Overall, the simulated FAS and PSA obtained from local site amplification estimated by the GIT perform better at most stations than the simulated values obtained from local site amplification estimated by the HVSR, which also indicates that the local site characteristics obtained by the GIT are closer to the actual geological conditions. In this study, we used data from different hypocentral distance ranges and the same magnitude ranges to calculate the local site effect in the study area, and the results show that the hypocentral distance has a small impact on the estimation of site amplification. In fact, the high-frequency component of the observation records is influenced by many factors, such as topography, site characteristics and environmental noise. In addition, the average high-frequency spectral decay parameter and near-surface site effect were used in our scheme, and all of these key parameters caused differences in the synthetic results to a certain extent.
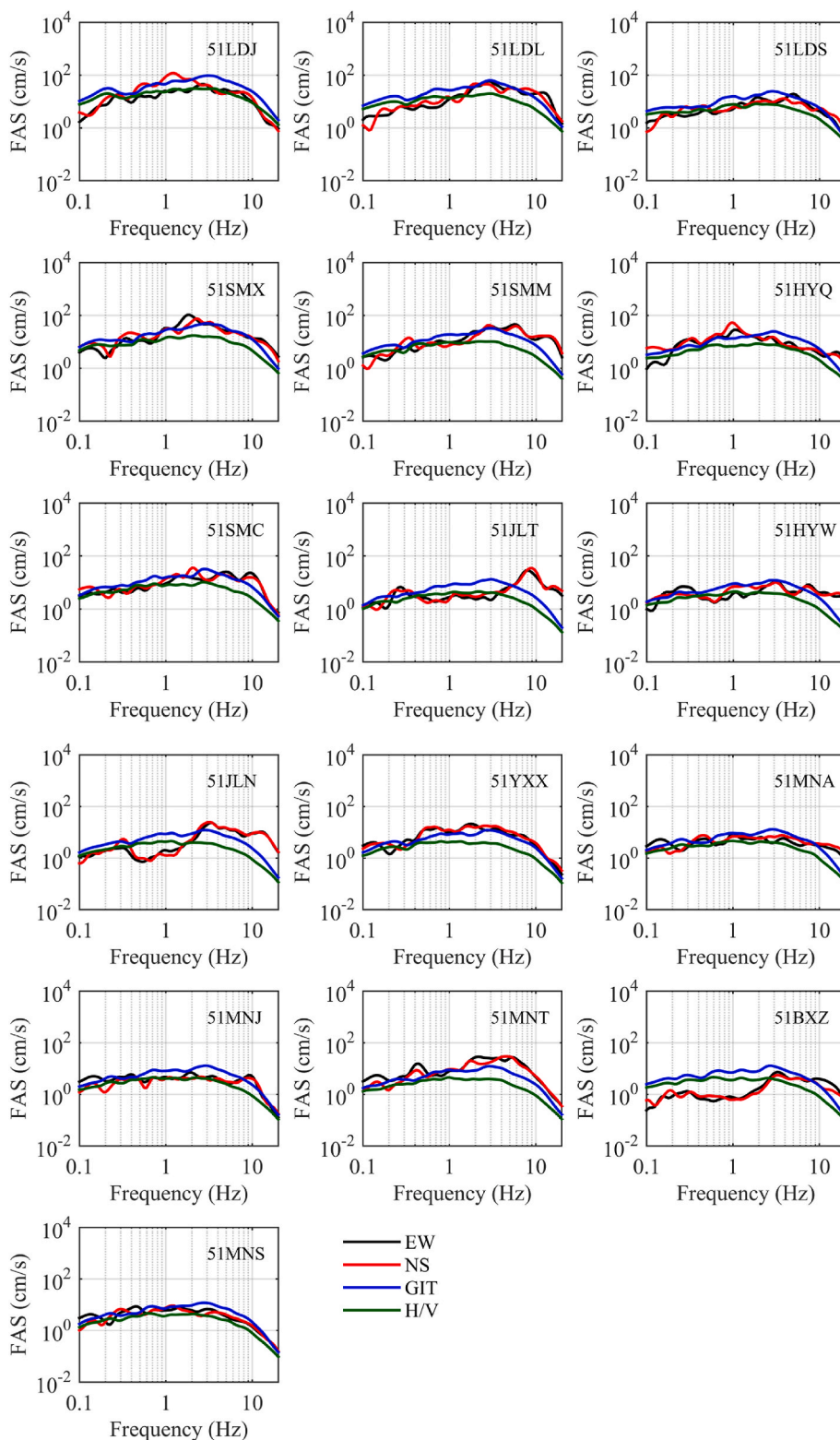
Fig. 5. Comparison of the simulated and observed FASs. The observed FAS in the EW and NS components and the simulated FAS obtained from the GIT and H/V spectral ratio methods were represented by black, red, blue and dark green solid lines, respectively.

4.2. Model bias

Fig. 7 shows the model bias, which can be given by the logarithmic difference between the simulated and recorded PSA obtained from the GIT and HVSR methods. Fig. 7 indicates that the model bias obtained from the GIT method is much nearer to the zero-reference lines than that

calculated by the HVSR at short periods, in which T is less than 1 s. In the range of 0.1–10 s, the model bias values calculated by the GIT are between −0.2 and 0.3, while the model bias values obtained by the HVSR are between −0.6 and 0.1, showing that synthetic and recorded PSA values exhibited little deviation within the range of periods considered in this simulation.
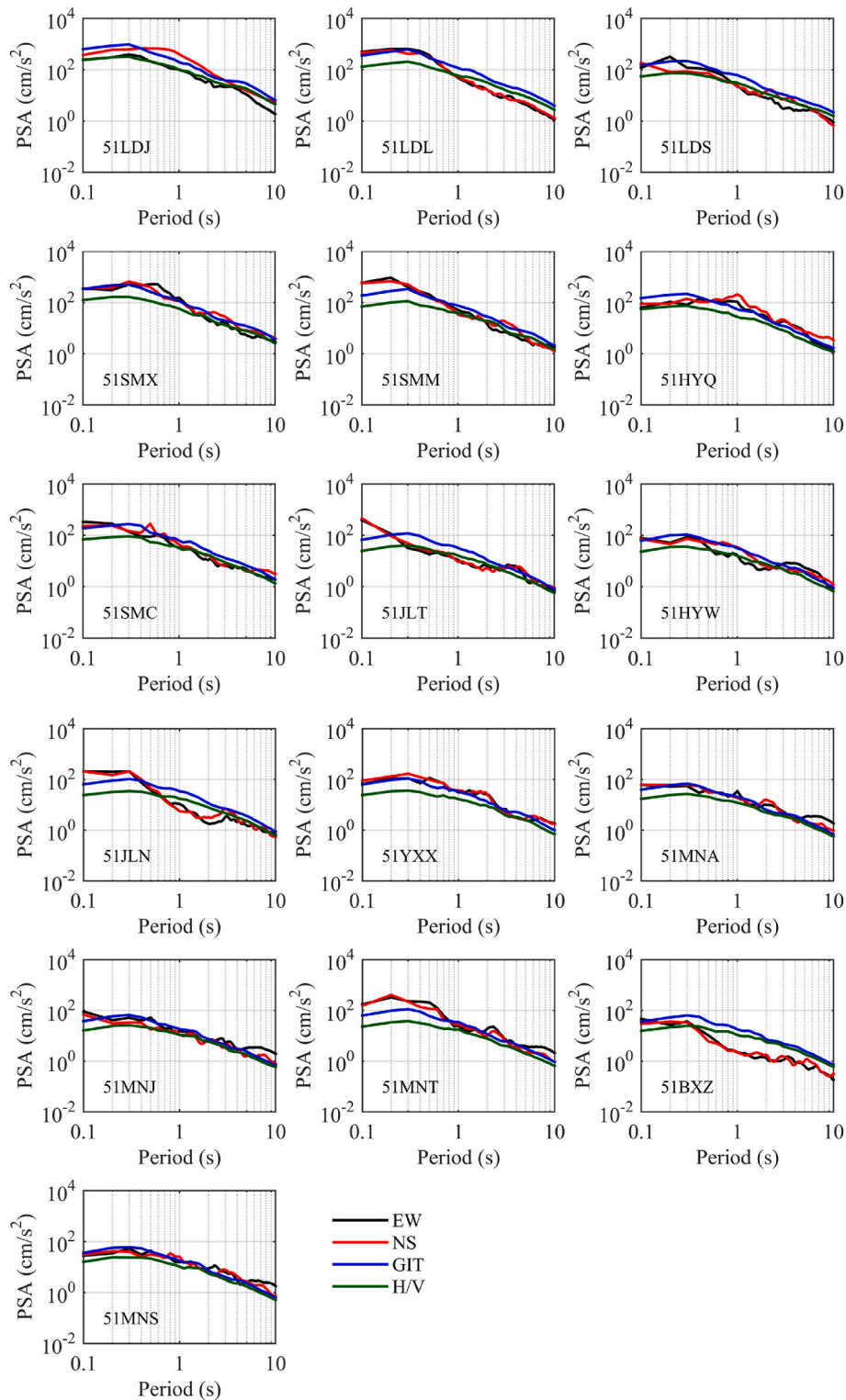
Fig. 6. Comparison of the synthetic and observed PSAs. The recorded PSA in the EW and NS components and the simulated PSA obtained from the GIT and H/V spectral ratio methods are represented by black, red, blue and dark green solid lines, respectively.

4.3. Comparison of the peak ground acceleration and velocity

Fig. 8 describes the comparison of the simulated PGA and peak ground velocity (PGV) values with the observed PGAs and PGVs, which clearly shows that the PGA and PGV values predicted by the GIT model can well match the recorded values at mid- and far-field stations with epicentral distances greater than 40 km. However, at these stations, the

PGAs and PGVs predicted by the HVSR model almost underestimate the recorded values, except for stations 51BXZ and 51MNS. At station 51LDJ, the PGA and PGV values predicted by both the GIT and HVSR models are between the two horizontal observations. However, at station 51LDL, the PGAs predicted by the GIT and HVSR models are 195.43 cm/s^2 and 71.9 cm/s^2, respectively. The predicted PGV values at station 51LDL are 13.924 cm/s (GIT) and 7.0122 cm/s (HVSR); the recorded
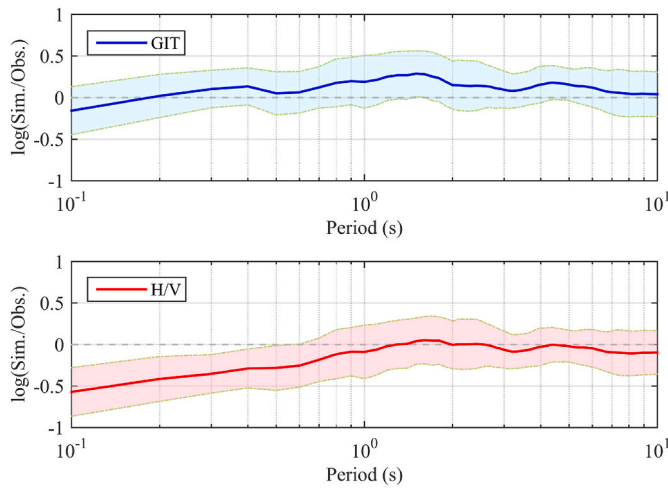
Fig. 7. Model bias calculated by the GIT method (upper panel) and H/V method (bottom panel). The shaded area represents the standard deviation range.

PGV values in the two horizontal components are 12.195 cm/s (EW) and 11.279 cm/s (NS). Fig. 9 shows the percentage of residual (POR) defined by the ratio of residual to observed values. The results indicate that the POR values of the PGA calculated by the GIT model are between −20% and 20% at most stations, and the POR values of the PGV calculated by the GIT model are between −30% and 30%. However, the POR values of the PGA calculated by the HVSR model are greater than 40%, and the POR values of the PGV calculated by the HVSR model are greater than 30%.

5. Conclusions

In this simulation, the widely used EXSIM algorithm [28,29] was adopted to model the FAS, PSA, PGA, and PGV values at 16 selected near-fault stations triggered by the 2022 Luding, China earthquake. Some input parameters, such as the local site amplification, quality factor and high-frequency attenuation parameter, were obtained via the strong-motion data of the earthquake, and the others were given by

previous studies. All these model parameters, including the source, site and path components, were collectively used to model the 2022 Luding earthquake occurred on September 5, 2022 in China. In our simulation, we attempted to investigate the impact of site amplification on the synthetic results; therefore, strong-motion recordings from different methods and distance ranges were used to estimate the local site amplification coefficients. The main conclusions can be summarized in detail as follows:

1. The 2568 sets of observation records from 81 strong-motion stations recorded by 161 earthquakes were used in the generalized inversion technique, and then the site effects were obtained. The results show that the dependence of site amplification on hypocentral distance is weak, and the historical strong-motion recordings of the study area can be used to estimate the near-surface site effect required for simulating scenario earthquakes. In addition, the site effects calculated by the HVSR approach is dramatically smaller than those estimated by the GIT approach, and it is necessary to enlarge the stress drop to obtain more accurate simulation results when performing EXSIM.

2. For the FAS, the local site amplification function obtained from the GIT can well match the recorded FAS at most stations. For the PSA, the site amplification estimated by the GIT can better match the observed PSA at most of the near-field stations, while the local site effects estimated by the HVSR method underestimate the observed PSAs, especially in the long period, in which period *T* is greater than 1 s. Besides, the comparison of the PGA and PGV shows that the PGA and PGV values predicted by the GIT can well match the recorded values at mid- and far-field stations with epicentral distances >40 km.

3. The inappropriate geometric spreading function and site amplification used in this study result in poor simulation results at some stations located in the distance range of 70 km–130 km. In addition, the synthetic results differ greatly from the recorded results at three near-field stations 51LDJ, 51LDL, and 51LDS may be resulted from the significant directivity effect of the rupture and the nonlinear characteristics of the site.

Although the calculation of some input parameters is not very accurate, overall, the source, path and site parameters determined in our scheme can model the ground motion characteristics of the selected
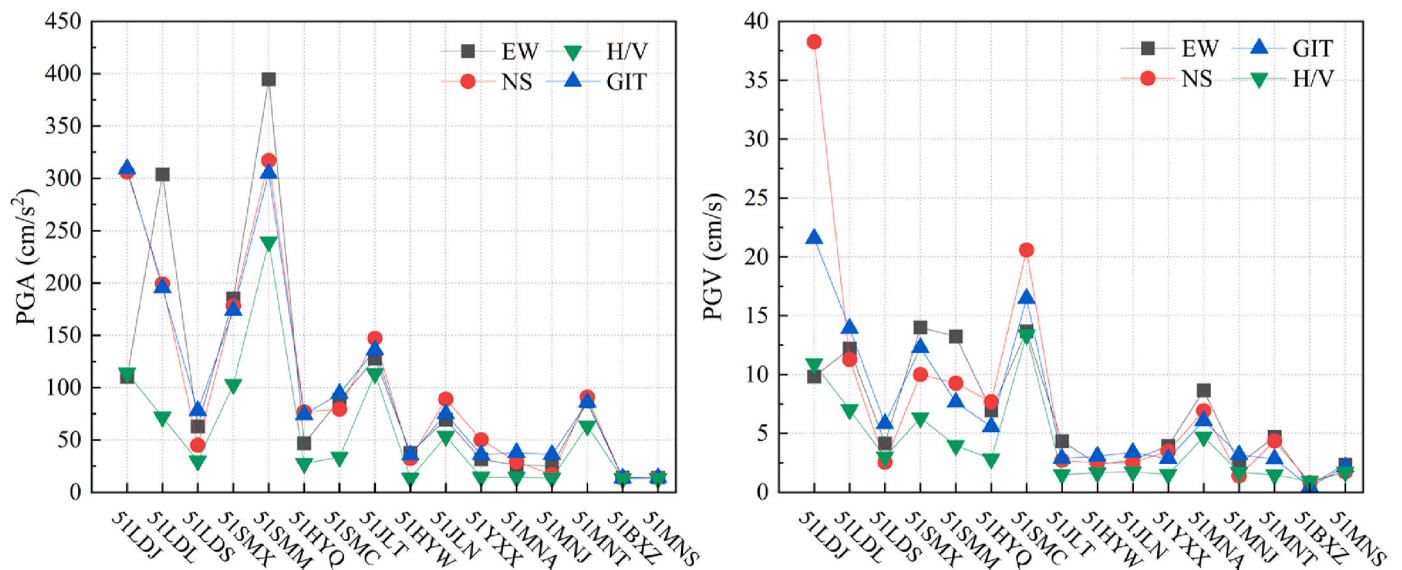

Fig. 8. Comparison of the simulated PGA (left panel) and PGV (right panel) obtained by the GIT and H/V methods with the observed values. Black rectangles, red circles and blue and green triangles represent the recorded values in the EW and NS components and the simulated values obtained from the GIT and H/V methods, respectively.
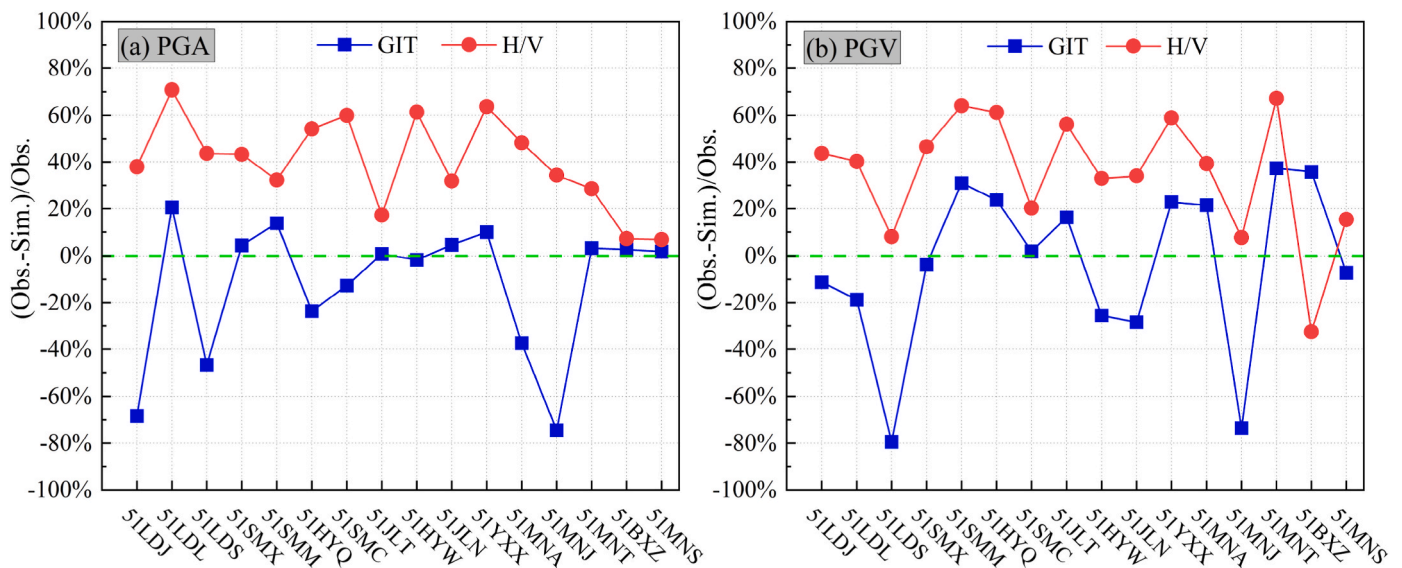
Fig. 9. Residual percentages between the PGA and PGV. Blue rectangles and red circles represent the values obtained from the GIT and H/V spectral ratio methods, respectively.

near-field stations during the Luding earthquake of Mw = 6.6 in China. In addition, our results indicate that regional site effects can be estimated using seismic records from nearby areas.

Data availability

The commonly used EXSIM code for simulation can be obtained from Prof. D. M. Boore's personal website at http://daveboore.com_www.daveboore.com/software_online.html (last accessed September 2018). Some source parameters are obtained from the Global Centroid Moment Tensor at https://www.globalcmt.org/(last accessed Oct. 20, 2021). The acceleration waveforms during the 2022 Mw 6.6 Luding earthquake were provided by the China Strong Motion Network Center at the Institute of Engineering Mechanics, China Earthquake Administration upon reasonable request. The slip distribution is given by Han et al. [61]. The macroseismic intensity map can be found at https://www.scdzj.gov.cn/dzpd/dzzj/scgzzldx_1662355316805/scgzzldx_1662355317416_yjcc_1662355319192/scgzzldx_1662355317416_yjtj_166235531 9442/202210/t20221021_53704.html (last accessed September 2023).

Some plots, such as Fig. 1, were made using the Generic Mapping Tools (GMT) software which can be downloaded from the website at https://www.gmt-china.org/download/(last accessed March 2023), and some figures, such as Figs. 2 and 5–7, were prepared using the MATLAB software which can be downloaded from the website at https://www.mathworks.cn/campaigns/products/trials.html (last accessed May 2018). The remaining figures were made using the Origin software (https://www.originlab.com/, last accessed May 2022).

Author contributions

All authors contributed to the study conception and design. Material preparation and data collection were performed by Pengfei Dang and Jian Song. Formal analysis was performed by Pengfei Dang, Hongfeng Yang and Jie Cui. The first draft of the manuscript was written by Pengfei Dang, all the figures were made by Pengfei Dang and all authors commented on previous versions of the manuscript. All authors read and approved the final manuscript.

Declaration of competing interest

The authors declare that they have no known competing financial interests or personal relationships that could have appeared to influence the work reported in this paper.

Data availability

The authors do not have permission to share data.

References

[1] Hinzen KG, Hinojosa-Prieto HR, Kalytta T. Site effects in archaeoseismic studies at mycenaean tiryns and midea. Seismol Res Lett 2016;87(5):1060–74.
[2] Woolery EW, Street R, Hart P, Padgett P. Two decades of linear site-effect observation (> 2 Hz) in the Wabash Valley, Central United Satates- context for the 2008 Illinois earthquakes sequence. Seismol Res Lett 2012;83(6):1090–103.
[3] Boore GM, Joyner WB. Site amplifications for generic rock sites. Bull Seismol Soc Am 1997;87(2):327–41.
[4] Boore DM. Simulation of ground motion using the stochastic method. Pure Appl Geophys 2003;160(3–4):635–76.
[5] Lermo J, Chavez-Garcia FJ. Site effect evaluation using spectral ratios with only one station. Bull Seismol Soc Am 1993;83(5):1574–94.
[6] Andrews DJ. Objective determination of source parameters and similarity of earthquakes of different size. In: Das S, Boatwright J, Scholz CH, editors. Earthquake source Mechanics, vol. 37. America Geophysical Union; 1986. p. 259–67.
[7] Ameri G, Oth A, Pilz M, Bindi D, Parolai S, Luzi L, Mucciarelli M, Cultrera G. Separation of source and site effects by generalized inversion technique using the aftershock recordings of the 2009 L'Aquila earthquake. Bull Earthq Eng 2011;9:717–39.

[8] Jeong SJ, Stump BW, DeShon HR. Spectral characteristics of ground motion from induced earthquakes in the Fort Worth basin, Texas, using the generalized inversion technique. Bull Seismol Soc Am 2020;110(5):2058–76.

[9] Castro RR, Pacor F, Bindi D, Franceschina G. Site response of strong motion stations in the Umbria, central Italy, region. Bull Seismol Soc Am 2004;94:576–90.

[10] Hassani B, Zafarani H, Farjoodi J, Ansari A. Estimation of site amplification, attenuation and source spectra of S-waves in the East-Central Iran. Soil Dynam Earthq Eng 2011;31:1397–413.

[11] Wang HW, Ren YF, Wen RZ. Source parameters, path attenuation and site effects from strong-motion recordings of the Wenchuan aftershocks (2008-2013) using a non-parametric generalized inversion technique. Geophys J Int 2018;212:872–90.

[12] Zafarani H, Hassani B, Ansari A. Estimation of earthquake parameters in the Alborz seismic zone, Iran using generalized inversion method. Soil Dynam Earthq Eng 2012;42:197–218.

[13] Zafarani H, Hassani B. Site responses and source spectra of S waves in the Zagros region, Iran. J Seismol 2013;17:645–66.

[14] Ren YF. Study on site effect in the Wenchuan earthquake using strong-motion recordings. Ph. D Thesis. Harbin: Institute of Engineering Mechanics, China Earthquake Administration; 2014 (in Chinese).

[15] Yu T, Li XJ. Inversion of strong motion data for source parameters of Wenchuan aftershocks, attenuation function and average site effect. Acta Seismol Sin (Engl Ed) 2012;34(5):621–32 (in Chinese).

[16] Wang HW, Wen RZ, Ren YF, Ji K. Estimating site response based on generalized inversion method for Lushan earthquake on April 20, 2013. Earthquake Eng. Eng. Dyn. 2014;34(4):35–41 (in Chinese).

[17] Zhou Y, Wang HW, Wen RZ, Miao TM, Cui JW. Source characteristics and path attenuation for the Yangbi, China seismic sequence in 2021. Pure Appl Geophys 2022;179:2721–33.

[18] Parolai S, Bindi D, Baumbach M, Karakisa S, Zünbül S. Comparison of different site response estimation techniques using aftershocks of the 1999 Izmit earthquake. Bull Seismol Soc Am 2004;94(3):1096–108.

[19] Bindi D, Parolai S, Cara F, Pacor F, Rovelli A. Site amplifications observed in the Gubbio basin, central Italy: hints for lateral propagation effects. Bull Seismol Soc Am 2009;99(2A):741–60.

[20] Parolai S, Bindi D, Augliera P. Numerical simulations and comparison with different site-estimation techniques. Bull Seismol Soc Am 2000;90(2):286–97.

[21] Zhang LB, Fu L, Liu AW, Chen S. Simulating the strong ground motion of the 2022 Ms6.8 Luding earthquake, Sichuan, China. Earthq Sci 2023;36(4):283–96.

[22] Xu XW, Zhang PZ, Wen XZ, Qin ZL, Chen GH, Zhu AL. Features of active tectonics and recurrence behavious of strong earthquakes in the western Sichuan Province and its adjacent regions. Seismol Geol 2005;27(3):446–61 (in Chinese).

[23] Wen XZ, Ma SL, Xu XW, He YN. Historical pattern and behavior of earthquake ruptures along the eastern boundary of the Sichuan-Yunan faulted-block, southwestern China. Phys Earth Planet In 2008;168(1–2):16–36.

[24] Huang YD, Xie CC, Li T, Xu C, He XL, Shao XY, Xu XW, Zhan T, Chen ZN. An open-accessed inventory of landslides triggered by the Ms6.8 Luding earthquake, China on September 5, 2022. Earthquake Res. Adv. 2022;3(1):100181.

[25] Yang ZG, Dai DQ, Zhang Y, Zhang XM, Liu J. Rupture process and aftershock focal mechanisms of the 2022 M6.8 Luding earthquake in Sicuan. Earthq Sci 2022;35(6):474–84.

[26] Zhou J, Xi N, Kang CC, Li L, Chen K, Tian X, Wang C, Tian JF. An accessible strong-motion dataset (PGA, PGV, and site Vs30) of 2022 M6.8 Luding, China earthquake. Earthq Sci 2023;36(4):309–15.

[27] Can G, Askan A, Karimzadeh S. An assessment of the 3 February 2002 Cay (Turkey) earthquake (Mw = 6.6): modeling of ground motions and felt intensity distribution. Soil Dynam Earthq Eng 2021;150:106832.

[28] Motazedian D, Atkinson GM. Stochastic finite-fault modeling based on a dynamic corner frequency. Bull Seismol Soc Am 2005;95(3):995–1010.

[29] Boore DM. Comparison stochastic point-source and finite-source ground-motion simulations: SMSIM and EXSIM. Bull Seismol Soc Am 2009;99(6):3202–16.

[30] Ghasemi H, Fukushima Y, Koketsu K, Miyake H, Wang ZF, Anderson JG. Ground-motion simulation for the 2008 Wenchuan, China, earthquake using the stochastic finite-fault method. Bull Seismol Soc Am 2010;100(5B):2476–90.

[31] Husid P. Gravity effects on the earthquake response of yielding structures, report of earthquake engineering Research laboratory. California Institute of Technology; 1967.

[32] McCann MWJ. Determining strong motion duration of earthquakes. Bull Seismol Soc Am 1979;69:1253–65.

[33] Moya A, Aguirre J, Irikura K. Inversion of source parameters and site effects from strong ground motion records using genetic algorithms. Bull Seismol Soc Am 2000;90(4):977–92.

[34] Drouet S, Chevrot S. Simultaneous inversion of source spectra, attenuation parameters, and site responses: application to the data of French accelerometric network. Bull Seismol Soc Am 2008;98(1):198–219.

[35] Konno K, Ohmachi T. Ground motion characteristics estimated from spectral ratios between horizontal and vertical components of microtremor. Bull Seismol Soc Am 1998;88(1):228–41.

[36] Castro RR, Fabriol H, Bour M, Le Brun B. Attenuation and site effects in the region of Guadeloupe, Lesser Antilles. Bull Seismol Soc Am 2003;93(2):612–26.

[37] Roumelioti Z, Benetatos C, Kiratzi A, Stavrakakis G, Melis N. A study of the 2 December 2002 (M 5.5) Vartholomio (western Peloponnese, Greece) earthquake and of its largest aershocks. Tectonophysics 2004;387:65–79.

[38] Taniran G, Yelkenci-Necmioglu S. Simulation of the strong ground motion for the 20 July 2017 (Mw 6.6) Bodrum-Kos earthquake. Bull Earthq Eng 2020;18:5807–25.

[39] Atkinson GM, Siddiqqi J. Ground-motion amplification at rock sites across Canada as determined from the horizontal-to-vertical components ratio. Bull Seismol Soc Am 2002;92(2):877–84.

[40] Parolai S, Richwalski SM. The importance of converted waves in comparing H/V and RSM site response estimates. Bull Seismol Soc Am 2004;94(1):304–13.

[41] Yaghmaei-Sabegh S, Hassani B. Investigation of the relation between Vs30 and site characteristics of Iran based on horizontal-to-vertical spectral ratios. Soil Dynam Earthq Eng 2020;128:105899.

[42] Dang PF, Cui J, Song J, Liu QF. Regional spectral characteristics, quality factor and site responses in western-central Sichuan, China (I): generalized inversion technique. Soil Dynam Earthq Eng 2023 (Under review).

[43] Dang PF, Cui J, Liu QF. Parameter estimation for predicting near-fault strong ground motion and its application to Lushan earthquake in China. Soil Dynam Earthq Eng 2022;156:107223.

[44] Yalcinkaya E, Pinar A, Uskuloglu O, Tekebas S, Firat B. Selecting the most suitable rupture model for the stochastic simulation of the 1999 Izmit earthquake and prediction of peak ground motions. Soil Dynam Earthq Eng 2012;42:1–16.

[45] Chopra S, Kumar D. Stochastic finite-fault modelling of Mw 4.8 earthquake in Kachchh, Gujarat, India. J Seismol 2012;16:435–49.

[46] Yaghmaei-Sabegh S, Tsang HH. A new site classification approach based on neural networks. Soil Dynam Earthq Eng 2011;31:974–81.

[47] Toni M. Simulation of strong ground motion parameters of the 1 June 2013 Gulf of Suez earthquake, Egypt. NRIAG J. Astro. Geophys. 2017;6:30–40.

[48] Mandal P, Dutta U. Estimation of earthquake source parameters in the Kachchh seismic zone, Gujarat, India, from strong-motion network data using a generalized inversion technique. Bull Seismol Soc Am 2011;101(4):1719–31.

[49] Ren YF, Wen WR, Yamanaka H, Kashima T. Research on site effect of Wenchuan earthquake by using generalized inversion technique. China Civ Eng J 2013;46 (S2):146–51 (in Chinese).

[50] Dang PF, Liu QF, Wang WB, Cui J. A revised stochastic finite-fault model based on the rupture process: a case study of the 2013 Mw 6.7 Lushan earthquake in China. Geophys J Int 2023 (Under Review).

[51] Ma WJ, Xie ZN, Zhang WY, Tang LH. Strong ground motion simulation of Lushan earthquake with a modified stochastic finite-fault method. Earthquake Eng. Eng. Dyn. 2021;41(5):123–33 (in Chinese).

[52] Yalcinkaya E. Stochastic finite-fault modeling of ground motions from the June 27, 1998 Adana-Ceyhan earthquake. Earth Planets Space 2005;57:107–15.

[53] Ghofrani H, Atkinson GM, Goda K, Assatourians K. Stochastic finite-fault simulations of the 2011 Tohoku, Japan, earthquake. Bull Seismol Soc Am 2013;103 (2B):1307–20.

[54] Safarshahi M, Rezapour M, Hamzehloo H. Stochastic finite-fault modeling of ground motion for the 2010 Rigan earthquake, southeastern Iran. Bull Seismol Soc Am 2013;103(1):223–35.

[55] Mittal H, Kumar A. Stochastic finite-fault modeling of Mw 5.4 earthquake along Uttarakhand-Nepal border. Nat Hazards 2015;75:1145–66.

[56] Mittal H, Wu YM, Chen DY, Chao QA. Stochastic finite modeling of ground motion for March 5, 2012, Mw 4.6 earthquake and scenario greater magnitude earthquake in the proximity of Delhi. Nat Hazards 2016;82:1123–46.

[57] Karimzadeh S, Ozsarac V, Askan A, Erberik MA. Use of simulated ground motions for the evaluation of energy response of simple structural systems. Soil Dynam Earthq Eng 2019;123:525–42.

[58] Atkinson GM, Assatourians K, Boore DM, Campbell K, Motazedian D. A guide to differences between stochastic point-source and stochastic finite-fault simulations. Bull Seismol Soc Am 2009;99(6):3192–201.

[59] Karashi J, Samaei M, Miyajima M. Finite-fault stochastic simulation of the 2008 Iwate-Miyagi Nairiku, Japan, earthquake. Nat Hazards 2022;114:1985–2912.

[60] Zafarani H, Rahimi M, Noorzad A, Hassani B, Khazaei B. Stochastic simulation of strong-motion records from the 2012 Ahar-Varzaghan Dual earthquakes, Northwest of Iran. Bull Seismol Soc Am 2015;105(3):1419–34.

[61] Han BQ, Liu ZJ, Chen B, Li ZH, Yu S, Zhang Y, Peng JB. Coseismic deformation characteristics of the 2022 Luding Mw 6.6 earthquake from InSAR and rupture slip distribution. Geomatics Inf Sci Wuhan Univ 2023;48(1):36–46 (in Chinese).

[62] Dang PF, Cui J, Liu QF, Li YD. Influence of source uncertainty on stochastic ground motion simulation: a case study of the 2022 Mw 6.6 Luding, China, earthquake. Stoch Environ Res Risk Assess 2023;37(8):2943–60.

[63] Beresnev IA. What we can and cannot learn about earthquake sources from the spectra of seismic waves. Bull Seismol Soc Am 2001;91(2):397–400.

[64] Dang PF, Cui J, Ma WJ, Li YD. Simulation of the 2022 Mw 6.6 Luding, China, earthquake by a stochastic finite-fault model with a nonstationary phase. Soil Dynam Earthq Eng 2023;172:108035.

[65] Dang PF, Cui J, Li Y, Wang WB. Simulation of ground motion from finite-fault modeling incorporating the influence of duration. Earth Space Sci 2023;10(8): 2023EA002871.

[66] Dang PF, Liu QF, Ma WJ, Wang C. Effects analysis of parameters on stochastically simulated ground motions. J. Dis. Prevention Mitigation Eng. 2022;42(4):768–77 (in Chinese).

[67] Atkinson GM, Boore DM. Ground-motion relations for eastern North America. Bull Seismol Soc Am 1995;85(1):17–30.

[68] Qiao HZ, Zhang YJ, Cheng WZ, Liu J. The inversion of the inelastic coefficient of the medium in North-West of Sichuan Province. Seismol. Geomagnetic Obs. Res. 2006;27(4):1–7 (in Chinese).

[69] Brune JN. Tectonic stress and the spectra of seismic shear waves from earthquake. J Geophys Res 1970;75(26):4997–5009.

[70] Ktenidou OJ, Gelis C, Bonilla LF. A study on the variability of Kappa (κ) for a sedimentary basin in Greece (EUROSEISTEST)—correlation to site characterization

parameters. In: Proc. Of the 15th world conf. Of earthquake engineering; 2013. Lisbon, Portugal, 4-28 September.

[71] Haendel A, Anderson JG, Pilz M, Cotton F. A frequency-dependent model for the shape of the Fourier amplitude spectrum of acceleration at high frequencies. Bull Seismol Soc Am 2020;110(6):2742–54.

[72] Nye T, Sahakian VJ, King E, Baltay A, Klimasewski A. Estimation of κ_0 and effect on ground motions in the San Francisco Bay area. Bull Seismol Soc Am 2023;113(2): 823–42.

[73] Fu L, Li XJ, Wang F, Chen S. A study of site response and regional attenuation in the Longmen Shan region, eastern Tibetan Plateau, SW China, from seismic recordings using the generalized inversion method. J Asian Earth Sci 2019;181:103887.

[74] Ugurhan B, Askan A, Akinci A, Malagnini L. Strong-ground-motion simulation of the April 2009 L'aquila, Italy, earthquake. Bull Seismol Soc Am 2012;102(4): 1429–45.

[75] Zengin E, Cakti E. Ground motion simulations for the 23 October 2011 Van, Eastern Turkey earthquake using stochastic finite fault approach. Bull Earthq Eng 2014;12:627–46.